Quantifying errors in surface ozone predictions associated with clouds over CONUS: A WRF-Chem modeling study using satellite cloud retrievals

Young-Hee Ryu[1], Alma Hodzic[1,2,*], Jerome Barre[1,a], Gael Descombes[1], Patrick Minnis[3]

[1]National Center for Atmospheric Research, Boulder, CO, USA

[2]Laboratoire d'Aérologie, Observatoire Midi-Pyrénées, CNRS, Toulouse, France.

[3]NASA Langley Research Center, Hampton, VA, USA

[a]now at: European Centre for Medium-Range Weather Forecasts, Reading, United Kingdom

[1,]Correspondence to A. Hodzic: **alma@ucar.edu***

Key words: surface ozone, photolysis, satellite clouds, WRF-Chem

Abstract

Clouds play a key role in radiation and hence O_3 photochemistry by modulating photolysis rates and light-dependent emissions of biogenic volatile organic compounds (BVOCs). It is not well known, however, how much error in O_3 predictions can be directly attributed to error in cloud predictions. This study applies the Weather Research and Forecasting with Chemistry (WRF-Chem) at 12 km horizontal resolution with the Morrison microphysics and Grell 3D cumulus parameterization to quantify uncertainties in summertime surface O_3 predictions associated with the cloudiness over contiguous United States (CONUS). All model simulations are driven by reanalysis of atmospheric data and reinitialized every 2 days. In sensitivity simulations, cloud fields used for photochemistry are corrected based on satellite cloud retrievals. The results show that WRF-Chem predicts about 55% of clouds in the right locations and generally underpredicts cloud optical depths. These errors in cloud predictions can lead up to 60 ppb overestimation in hourly surface O_3 concentrations on some days. The average difference in summertime surface O_3 concentrations derived from the modeled clouds and satellite clouds ranges from 1 to 5 ppb for maximum daily 8-h average O_3 (MDA8 O_3) over CONUS. This represents up to ~40% of the total MDA8 O_3 bias under cloudy conditions in the tested model version. Surface O_3 concentrations are sensitive to cloud errors mainly through the calculation of photolysis rates (for ~80%), and to a lesser extent to light-dependent BVOC emissions. The sensitivity of surface O_3 concentrations to satellite-based cloud corrections is about 2 times larger in VOC-limited than NO_X-limited regimes. Our results suggest that the benefits of accurate predictions of cloudiness would be significant in VOC-limited regions which are typical of urban areas.

1. Introduction

Ozone (O_3) is a secondary pollutant that is formed by chemical reactions involving nitrogen oxides ($NO_X = NO + NO_2$) and volatile organic compounds (VOCs) in the presence of ultraviolet radiation. Because O_3 is a harmful pollutant and a greenhouse gas, there have been numerous efforts aimed at improving O_3 predictions in air quality models, i.e. through a better characterization of the emissions of O_3 precursors (Brioude et al., 2013), more detailed chemical mechanisms (Carter, 2010; Sarwar et al., 2013), more realistic lateral boundary conditions (e.g., Tang et al., 2009), and improved representation of meteorological fields with ensemble modeling techniques (Bei et al., 2010; Zhang et al., 2007). A comprehensive review of the current status and challenges of air quality forecasting is given by Zhang et al. (2012). A large O_3 bias that still persists in most regional and global models is one of the challenges (Brown-Steiner et al., 2015; Fiore et al., 2009; Im et al., 2015; Lin et al., 2017; Travis et al., 2016). The recent multi-model intercomparison study by Im et al. (2015) indicates that over North America models tend to overestimate hourly surface O_3 below 30 ppb by 15–25% and to underestimate O_3 levels above 60 ppb by up to ~80%. It is not quantitatively understood how much the individual processes contribute to O_3 biases. Among meteorological parameters, clouds can be one of the key factors because they greatly modulate the ultraviolet radiation that is critical for O_3 formation. However, they remain one of the largest sources of uncertainties in air quality modeling as Dabberdt et al. (2004) pointed out a decade ago. Accurate cloud predictions in numerical weather models are still challenging, and it has not yet been quantified how much errors in cloud prediction impact surface O_3 predictions.

As satellite cloud products have emerged, providing reasonably accurate data with wide coverage and high temporal resolutions in near-real time (e.g., Minnis et al., 2008), they have

63 been employed in various studies to quantify the effects of clouds on actinic fluxes and/or

64 photolysis rates (Mayer et al., 1998; Ryu et al., 2017; Thiel et al., 2008). Clouds can greatly

65 reduce or enhance actinic flux below, above, and inside clouds, and these effects depend mainly

66 on the cloud optical properties. Ryu et al. (2017) used satellite cloud retrievals of cloud bottom

67 and top heights and cloud optical depth (COD) in a radiative transfer model, and showed that one

68 can obtain fairly good (within ±10%) vertical distributions of cloudy-sky actinic flux using

69 satellite cloud properties. There are, however, only a limited number of studies that have

70 examined the impact of satellite-constrained clouds and photolysis rates on O_3 formation. Pour-

71 Biazar et al. (2007) and Tang et al. (2015) used satellite-observed clouds to correct photolysis

72 rates in a three-dimensional chemistry transport model and reported considerable improvement

73 in surface O_3 simulations. Pour-Biazar et al. (2007) showed that the difference in O_3 due to the

74 errors in cloud predictions can be up to 60 ppb for a given pollution episode over the south US.

75 Tang et al. (2015) showed that 1-month averages of 8-h surface O_3 can differ by 2–3 ppb

76 between the simulations using satellite-derived clouds and model-predicted clouds over the south

77 US. These studies were performed for rather short time periods (a week or a month) over limited

78 areas, and provide motivation for a more systematic/comprehensive quantification of the

79 importance of cloud errors in O_3 predictions in summertime and for various chemical regimes.

80 In the present study, we use satellite-derived COD and cloud boundaries to constrain radiation

81 fields that impact photochemistry, i.e., photolysis rates and light-dependent BVOC emissions, in

82 a three-dimensional chemistry transport model (WRF-Chem). Our study targets the contiguous

83 United States (CONUS) and numerical simulations are performed for June–September 2013. The

84 WRF-simulated clouds are first evaluated against the Geostationary Operational Environmental

85 Satellite (GOES) data (section 3). The vertical profiles of NO_2 photolysis rates are evaluated

86   against in-situ airborne measurements during two field campaigns (section 4). The O_3 biases

87   arising from inaccurate cloud predictions are quantified, and discussed in light of the sensitivity

88   of O_3 chemistry to COD (section 5). Unlike the previously mentioned studies, here we quantify

89   separately the contributions of errors arising from changes in photolysis rates altered by clouds

90   vs. those arising from light-dependent BVOC emissions to the O_3 biases. Conclusions and

91   discussion are given in section 6.

92   ## 2. Methodology

93   ### 2.1. Satellite retrievals

94   The GOES retrievals were performed using the Satellite ClOud and Radiation Property Retrieval

95   System (SatCORPS), which is an adaptation of the Minnis et al. (2011) algorithms for

96   application to imagers on all geostationary weather satellites (Minnis et al. 2008) and on NOAA

97   and MetOp satellites (Minnis et al. 2016). For SatCORPS, the algorithms of Minnis et al. (2011)

98   were altered as described by Minnis et al. (2010) using the low-cloud height estimation method

99   of Sun-Mack et al. (2014) and the severely roughened hexagonal column optical model of Yang

100   et al. (2008) for ice cloud COD retrievals. This study uses a subset of the hourly, 8-km

101   SatCORPS cloud retrievals from GOES 13 (GOES-East) and GOES 15 (GOES-West) for the

102   North American domain. The 8-km resolution is achieved by analyzing only every other 4-km

103   pixel and line. Each pixel is considered to be either 100% cloudy or 100% clear. Of the variety of

104   cloud properties available, this study only uses cloud bottom height, cloud top height, and COD.

105   Uncertainties in the cloud products are summarized by Ryu et al. (2017).

106   Images from coincident times were unavailable for the two satellites: the GOES 13 and GOES

107   15 data are offset by 15 min. The GOES 13 data taken at UTC + 45 min at every hour were

108   matched with the GOES 15 data at UTC + 00 min. The pixel-level retrievals were re-gridded to a

109   12-km resolution to match the WRF-Chem domain (see section 2.2) using the Earth System

110   Modeling Framework (ESMF) software and the nearest-neighbor interpolation. Because of the

111   coverage difference between the two satellites, the data of the nearest time from the two satellites

112   (e.g., 1845 UTC from GOES 13 and 1900 UTC from GOES 15) are merged at 105°W, which is

113   equidistant from the two sub-satellite longitudes. Only daytime hours (09–23 UTC and 00–04

114   UTC) are used here.

115

2.2. WRF-Chem model simulations

117   The present study employs the WRF-Chem model version 3.6.1. with the updated photolysis

118   scheme. A single domain is used with a horizontal grid size of 12 km (Fig. 1). The

119   meteorological initial and boundary conditions are provided by the NCEP FNL (Final)

120   Operational Global Analysis data with a horizontal resolution of 1°, which are available every 6

121   hours. The model is initialized at 00 UTC 1 June 2013 and spun-up for the first 10 days in the

122   control simulation (CNTR simulation). The meteorological fields are re-initialized every 48

123   hours at 06 UTC of a given day to avoid the growth of model errors, and the model is run for 54

124   hours. Here, the first 6 hours are allowed for spin-up and discarded in each run. The model

125   outputs for the period of 12 UTC 11 June 2013 through 12 UTC 1 October 2013 are used for the

126   analysis. As the goal of the study is to use and evaluate the modeled clouds and their impact on

127   O_3 predictions, nudging is not used. This is different from many previous air quality studies that

128   nudged the meteorology and evaluated modeled O_3 with observations. The physics options used

129   are the Morrison two-moment scheme (Morrison et al., 2009) for the microphysics, RRTMG

130   scheme for longwave and shortwave radiation (Iacono et al., 2008), MYNN 2.5 level TKE

131 scheme for the boundary layer parameterization (Nakanishi and Niino, 2006), MYNN surface

132 layer scheme, Noah land surface model (Chen and Dudhia, 2001), and Grell 3D ensemble

133 scheme (Grell and Devenyi, 2002) for cumulus parameterization with radiation feedback. The

134 initial and boundary conditions for chemical species are obtained from the Model for OZone And

135 Related chemical Tracers (MOZART) global simulation of trace gases and aerosols. For each 2-

136 day simulation, the chemical state of the atmosphere at 06 UTC is obtained from that at 06 UTC

137 of the previous simulation. The MOZART-4 mechanism is used for gas-phase chemistry as

138 described in Knote et al. (2014), and the Model for Simulating Aerosol Interaction and

139 Chemistry (MOSAIC) aerosol module with 4 bins is used for the aerosol chemistry.

140 Anthropogenic gas and aerosol emissions are adopted from the AQMEII project in which the

141 emissions were projected to 2010 from the NEI 2008 inventory (Campbell et al., 2015). Since

142 Travis et al. (2016) reported that NEI NO_X emissions are too high, we reduced NO_X emission

143 from all anthropogenic sources by 40% based on their analysis. Note that the NO_X and PAN

144 from the lateral boundaries are also reduced by 40% in our study. Biomass burning emissions are

145 taken from the Fire Inventory from NCAR (FINN) (Wiedinmyer et al., 2011). Model of

146 Emissions of Gases and Aerosols from Nature (MEGAN) (Guenther et al., 2006) version 2.04 is

147 used for BVOC emissions. As done in Travis et al. (2016) to better match isoprene flux

148 observations during the Studies of Emissions and Atmospheric Composition, Clouds and Climate

149 Coupling by Regional Surveys (SEAC[4]RS) field campaign (Toon et al., 2016), we reduced

150 MEGAN isoprene emissions by 15% over the southeast US. The photolysis rate calculations

151 utilize the newly implemented TUV option in the WRF-Chem model (Hodzic et al., 2017 in

152 preparation). This new TUV option uses the updated cross section and quantum yield data based

153 on the latest stand-alone TUV model version 5.3, and considers 156 wavelength bins with the

154 resolutions of 1−5 nm. The COD is calculated based on the parameterization given in Chang et al.

155 (1987), which uses cloud liquid water and/or ice water contents and effective droplet radius

156 (assumed to be 10 μm both for liquid and ice droplets). To represent subgrid cloud overlaps, a

157 simple equation of Briegleb (1992) is used, i.e., the effective $COD = COD_0 \times (cloud\ fraction)^{1.5}$,

158 where COD_0 is the cloud optical depth that is calculated following Chang et al. (1987), and the

159 cloud fraction is determined based on the relative humidity in a given grid box. According to

160 Briegleb (1992), applying a power of 1.5 to the cloud fraction is equivalent to the maximum

161 random overlap.

162 In the present study, we performed two sets of simulations that use WRF generated clouds in the

163 CNTR simulation and the GOES clouds in the GOES simulation. The GOES simulations are

164 conducted from 06 UTC 11 June 2013 through 12 UTC 1 October 2013. The initial chemistry

165 conditions in the GOES simulation are adopted from the outputs of the CNTR simulation at 06

166 UTC 11 June 2013. The satellite cloud retrievals are used only to correct photolysis rate and

167 photosynthetically active radiation (PAR) calculations (i.e., only within the TUV model in WRF-

168 Chem). That is, the satellite cloud information is not linked to dynamics, microphysics, and

169 atmospheric radiation. The value of COD is linearly distributed through vertical grids from the

170 cloud bottom to the cloud top within the TUV model as done in Ryu et al. (2017). This method is

171 different from the one used in Pour-Biazar et al. (2007) and Tang et al. (2015) in which cloud

172 bottom height used in their photolysis rate calculations is estimated from the meteorological

173 model rather than retrieved from the satellite. The use of model estimates can lead to additional

174 uncertainties in the case of misplaced model clouds compared to observations.

175 In the present study, PAR calculated from the TUV model is used for the BVOC emissions in

176 MEGAN for all simulations. This is different from the PAR conventionally used in MEGAN,

177   which is simply converted/scaled from the downward shortwave radiation from the atmospheric

178   radiation scheme. In the CNTR (GOES) simulation, the WRF generated clouds (GOES clouds)

179   are used for the PAR calculation within the TUV model.

180   To examine the impact of changes in BVOC emissions on surface O_3, another set of sensitivity

181   simulation (EMIS_BVOC simulation) is performed for 10 days (3–12 July 2013), which uses

182   WRF-generated clouds for the PAR calculation and BVOC emissions as in the CNTR simulation

183   but uses the GOES clouds for photolysis rate calculations as in the GOES simulation. The

184   description of the control and sensitivity simulations is summarized in Table 1.

185

2.3. Observational data

2.3.1. Aircraft data from field campaigns

188   We evaluate the model performance using airborne measurements made during two field

189   campaigns in 2013, i.e., the NOMADSS (Nitrogen, Oxidants, Mercury and Aerosol Distributions,

190   Sources and Sinks) and the SEAC[4]RS campaigns. The detailed description of the instrument and

191   measurement data is given in Ryu et al (2017). The NOMADSS campaign was conducted during

192   1 June–15 July 2013 mainly over the southeast US. We use 16 flight-day data at 1-min time

193   intervals for the analysis. Data with solar zenith angles larger than 85° are not used. The fire

194   plume data are filtered out by excluding the data showing NO_2 (> 0.1 ppb) or CO (> 120 ppb)

195   aloft at 4–7 km level. Based on the GOES cloud data, 68% of flight data are characterized by

196   clear skies and the remaining data (32%) had clouds in the vertical column where the airplane

197   was located. The SEAC[4]RS campaign also targeted the southeast US although the airplane

198   sometimes flew over a larger region including California and Midwestern US. The period used

199   for the analysis is from 6 August through 23 September 2013, which includes 21 flight days. The

200   time intervals are also 1-min and the data with large solar zenith angles ($> 85°$) and fire plumes

201   are filtered out. The fraction of data with clouds is 41% for SEAC^{4}RS. It is noteworthy that

202   SEAC^{4}RS measurements include large and thick clouds in some cases as a few of the campaign

203   goals are to identify the role of deep convection in redistributing pollutants and aerosol-clouds

204   feedbacks, whereas the clouds during NOMADSS were mostly broken clouds.

205   *2.3.2.   Ground ozone data*

206   The United States Environmental Protection Agency (EPA) hourly O_3 measurements are used for

207   the analysis. To examine the sensitivity of O_3 to COD in different chemical regimes, the VOC-

208   and NO_X-limited regimes are identified using the ratio of $\Delta O_3/\Delta NO_y$, following Sillman and He

209   (2002). They reported that the NO_X-VOC transition occurs when $\Delta O_3/\Delta NO_y = 4$–6. Thus, an

210   EPA site is denoted as a VOC-limited (NO_X-limited) regime when the ratio is less than 4 (greater

211   than 6). Examples showing the ratio of $\Delta O_3/\Delta NO_y$ for several sites are given in the

212   supplementary materials (Fig. S1). Among 1,299 EPA sites, 1,062 are used for the analysis: 24%

213   of the sites are in the VOC-limited and 76% in NO_X-limited regimes. The remaining 237 sites are

214   not used in the present study because those sites fall into the transitional zone, i.e., $\Delta O_3/\Delta NO_y =$

215   4–6. Note that modeled O_3 and NO_y in the CNTR simulation are used to determine whether an

216   EPA site is in VOC-limited or NO_X-limited regime because NO_y measurements are available for

217   limited sites.

218   # 3. Evaluation of WRF clouds with satellite measurements

219   The model bias in the cloud spatial coverage is evaluated using a 2×2 contingency table (Table

220   2), where A and D correspond to hit and correct negative events, respectively, and B and C to

221 false alarm and miss events, respectively. Here, a threshold of 0.3 in hourly COD is used to

222 distinguish between clear and cloudy sky as the lowest detection limit of satellite retrieved COD

223 over land is estimated to 0.25 in Rossow and Schiffer (1999), and the use of 0.3 poses slightly

224 stricter conditions for cloudiness. The agreement index, which is defined as A+D (WRF predicts

225 correctly cloudy or clear skies), is 69.7% and the probability of detection (POD) for clouds,

226 A/(A+C), is 55.6%. It is found that the fraction of errors in missing clouds (C, 19.8%) is larger

227 than that of predicting clouds that are not present in reality (B, 10.4%). The overall bias,

228 (A+B)/(A+C), is 0.789 and this means that the WRF underestimates the frequency of cloudy

229 skies. Figure 1 shows the spatial distribution of each contingency category over the CONUS

230 averaged over the whole study period. In general, the eastern US shows higher cloud frequencies

231 than the western US except for parts of the Rocky Mountains and the Pacific Northwest. The

232 largest agreement index appears in central California where the sky condition is mostly clear (Fig.

233 1d). In terms of errors, the missing clouds rate has its highest frequency (20−35%) in the

234 Midwestern and northwestern US, while the highest frequency of false alarm (20–30%) occurs

235 over the southeast US and the southeastern Texas. The sum of category B and C can be found in

236 the supplementary material (Fig. S2). It should be noted that the contingency categories are

237 based on binary results of cloud-free or cloudiness and so they do not provide quantitative

238 comparison of cloud optical properties, e.g., COD. For example, even though the WRF model

239 produces clouds in the right locations (category A), the WRF CODs can differ from those

240 retrieved from satellite data.

241 Figure 2 evaluates quantitatively COD and vertical extent of clouds between the model and

242 satellite retrievals. The vertical extent of clouds is classified based on the International Satellite

243 Cloud Climatology Project (ISCCP) definition (Rossow and Schiffer, 1999), which are as

244   follows: i) low-level: cloud top height ≤ 3 km, ii) mid-level: 3 km < cloud top height ≤ 6 km, iii)

245   high-level: cloud bottom height > 6 km, and iv) multi-layered or deep convection: cloud bottom

246   height ≤ 6 km and cloud top height > 6 km. Even though multiple cloud layers can be resolved in

247   the WRF model, these kinds of clouds are not resolved in the satellite retrievals used in this study.

248   Thus, for a fair comparison, the multi-layered clouds in the WRF model are not further resolved

249   into cloud layers. Note that the liquid/ice water contents from cumulus clouds (parameterized

250   clouds) are included in the model COD calculations.

251   The frequency distribution of CODs does not have the same shape in the model and observations.

252   The WRF model overpredicts by a factor of 2 very thin clouds with COD < 1, whereas the

253   GOES retrievals show that the most abundant clouds have CODs of 2–5. The majority of

254   optically very thin clouds from the WRF model correspond to high-level cirrus clouds. This is

255   consistent with the result of Cintineo et al. (2013), showing that the Morrison microphysics

256   scheme produces too many upper-level clouds by comparing GOES infrared brightness

257   temperature with the WRF model. Note that the optically-thin multi-layered clouds very likely

258   contain cirrus clouds because their top height is greater than 6 km. The WRF model produces

259   fewer clouds with COD > 1 than observed, and the discrepancy is most apparent for optically

260   very-thick clouds (COD > 50). As a result, the model COD mean and standard deviation are

261   smaller than those for the retrievals, which are 8.3 and 12.7, respectively for the WRF model,

262   and 17.8 and 30.8, respectively for the GOES retrievals.

263   **4. Impact of cloud errors on photolysis rates**

264   Figure 3 compares the cloudy-sky averaged vertical profiles of NO_2 photolysis rates (JNO_2)

265   predicted by WRF-Chem and measured during the NOMADSS (Fig. 3a) and SEAC[4]RS (Fig. 3d)

266   campaigns. The histograms of ratio of JNO_2 simulated to that observed under cloudy conditions

267   are also shown for the CNTR and GOES simulations.

268   For both campaigns, the simulations with satellite clouds (GOES simulations) generally show

269   better agreement with the observed JNO_2 profiles than the CNTR simulations, especially above

270   the boundary layer (above ~2 km). The histograms of the ratio model-to-observation JNO_2 also

271   show a better performance generally in the GOES simulation than in the CNTR simulation: the

272   mean of the ratio is closer to 1 in the GOES simulation than in the CNTR simulation for

273   SEAC[4]RS, the standard deviations are reduced in the GOES simulation compared to those in the

274   CNTR simulation for both campaigns, the root-mean-square-errors are lowered in the GOES

275   simulation compared to those in the CNTR simulation, and the correlation coefficients are closer

276   to 1 in the GOES simulation than in the CNTR simulation. For NOMADSS, the large bias in the

277   highest ratio bin (> 2) is 24% less in the GOES simulation than in the CNTR simulation. The

278   reduction of the large bias (bin > 2) in the GOES simulation is more substantial for SEAC[4]RS

279   and reaches 47%. These reductions are attributed to a better representation of the below-cloud

280   and inside-cloud conditions when satellite clouds are used (not shown). This is because the

281   number of data influenced by thick clouds is larger in SEAC[4]RS than in NOMADSS and the

282   measurements in the presence of those thick clouds were mostly made under below-cloud or

283   inside-cloud conditions.

5. Impact of cloud errors on ground level ozone

284

5.1. An example on 8 July 2013 in Midwestern US

285

286   Figure 4 shows an example of how model errors in cloud fields impact O_3 predictions. This

287   example includes thunderstorm systems over the Midwestern US. The CNTR simulation misses

288 clouds or underpredicts CODs over metropolitan Chicago and the region south of Lake Michigan.

289 This results in the overprediction of JNO_2 by up to 0.54 min^{-1} (~90%) compared to that

290 computed using GOES clouds. The resulting changes in O_3 concentration are regional and the O_3

291 overprediction in the plume originating from the Chicago area is up to 62 ppb (~60% of O_3 in the

292 CNTR simulation). As a result of the cloud corrections, O_3 in the GOES simulation agrees better

293 with observations in those regions (compare Fig. 4d with Fig. 4e and Figs. 4g,h,i). The time

294 series of O_3 at the three sites (marked in Fig. 4f) near Lake Michigan show particularly improved

295 agreement with observations when satellite clouds are used. The large O_3 biases of 20.5 ppb at

296 11 CST at Chicago, IL, 19.2 ppb at 13 CST at La Porte, IN, and 23.5 ppb at 16 CST at Holland,

297 MI in the CNTR simulation are reduced to 1.7 ppb, 3.2 ppb, and −0.11 ppb in the GOES

298 simulation, respectively. It is also apparent that the bias reduction in O_3 shifts eastward (from

299 Chicago, IL to Holland, MI) as the thunderstorm moves eastward during the day. An important

300 implication of this finding is that errors in cloud predictions can lead to wrong O_3 alerts in areas

301 where model does not predict clouds well. For example, the maximum daily 8-h average O_3

302 (MDA8 O_3) concentration is 75.3 ppb at Holland, MI in the CNTR simulation (Fig. 4i) and this

303 value exceeds the O_3 standard (70 ppb for MDA8 O_3). However, the MDA8 O_3 concentration at

304 the same location is 63.0 ppb in the GOES simulation and 60.4 ppb in the observation. Therefore,

305 an O_3 action alert would have been issued if the CNTR simulation results are used, which results

306 in a false alarm. The example shown here emphasizes the important roles of clouds in the Great

307 Lakes region where large O_3 biases have been reported previously in air quality forecasts (e.g.,

308 Cleary et al., 2015). The correction of clouds both over the lakes and in the upstream regions

309 (mostly large cities located to the west/southwest of the lakes) significantly reduces the O_3 bias.

310 It is also shown that polluted air masses from the source regions can be advected over the lakes

311 (not shown). In this case in which precursor levels can be high over the lakes, the presence of

312 clouds over the lakes can greatly affect O_3 formation over the lakes.

313 In general, the regions exhibiting O_3 differences between the two simulations coincide with the

314 regions where JNO_2 values are different. More importantly, large O_3 differences are found near

315 urban areas (e.g., Chicago, IL; downwind area of Kansas City, MO; Omaha, NE and its

316 downwind area). Even though the difference in COD or JNO_2 is significant in central Indiana,

317 for example, the difference in O_3 in the region is relatively small compared to that near Lake

318 Michigan.

319

320 **5.2. Maximum daily 8-h average O_3**

321 Figure 5 shows the maps of MDA8 O_3 averaged over the study period for the CNTR simulation

322 and the difference in MDA8 O_3 between the CNTR and GOES simulations. The spatial

323 distribution of MDA8 O_3 in the GOES simulation is similar to that in the CNTR simulation (thus

324 the GOES spatial average is not shown here), but the O_3 levels are considerably different. In Fig.

325 5b, the Midwestern, eastern, and northwestern US regions show the largest O_3 differences, up to

326 5.8 ppb, with lower O_3 levels in the GOES simulation. These regions generally belong to the

327 contingency category C (Midwestern and northwestern US) or category A (eastern US). On the

328 other hand, the regions with negative differences, i.e., some places over the south/southeastern

329 US, coincide with the contingency category B. These differences are expected and can be

330 interpreted as follows: when the WRF model misses clouds (clear sky in the CNTR simulation,

331 category C) or underestimates COD (as seen in Fig. 2), surface O_3 is overestimated. When the

332 WRF model generates clouds that are not present in reality (clear sky in the satellite retrievals,

333 category B), surface O_3 is underestimated. It should be noted that not all regions belonging to

334 category B or C have significant O_3 differences. Interestingly, the regions exhibiting significantly

335 large O_3 differences coincide with large urban areas, e.g., Seattle, WA; Los Angeles, CA;

336 Chicago, IL; Cleveland, OH; Houston, TX; New Orleans, LA; Atlanta, GA; and Miami, FL. The

337 reasons for this result are explored in section 5.4 and 5.5.

338 The performance of the GOES simulation is found to be better than that of the CNTR simulation

339 as compared to observations: for example, under cloudy conditions (COD > 20, see section 5.4

340 for the criterion), the root-mean-square error of MDA8 O_3 in the GOES (CNTR) simulation is

341 13.2 ppb (16.9 ppb) and the correlation coefficient of MDA8 O_3 in the GOES (CNTR)

342 simulation is 0.5 (0.4).

343 **5.3. Relative contribution to O_3 errors from photolysis rates and BVOC emissions**

344 It is expected that reduced BVOC emissions (especially isoprene) due to the presence of clouds

345 can also decrease O_3 formation. Figure 6 shows the spatial distributions of relative changes in

346 PAR and isoprene emission between the EMIS_BVOC and GOES simulations averaged over a

347 10-day period. Because the WRF model tends to underestimate COD or is not able to reproduce

348 clouds in Midwestern and western US, PAR and biogenic isoprene emissions are larger in the

349 EMIS_BVOC simulation than in the GOES simulation. On the other hand, the model

350 overestimates COD or produces clouds that are not present in reality over the southeast US, so

351 PAR and biogenic isoprene emissions are lower in the EMIS_BVOC simulation than in the

352 GOES simulation. The change in PAR (biogenic isoprene emissions) resulting from the

353 difference in clouds fields between the WRF model and satellite retrievals is up to ±30–40%

354 (±25%). Figure 6d shows the relative O_3 difference between EMIS_BVOC and GOES

355 simulations to O_3 difference between CNTR and GOES simulations (Fig. 6c). It is seen that the

356 contribution of changes in BVOC emissions is considerable only for some regions and it ranges

357   from ~10–40%. The average contribution of changes in BVOC emissions over land is ~20%

358   compared to changes of BVOC emissions plus photolysis rates using GOES satellite clouds. The

359   contribution of BVOC emissions is larger (~40%) in urban areas over the southeast (specifically

360   in Charlotte, NC). The difference in O_3 in Charlotte, NC resulting from changes in BVOC

361   emissions is about 1.5 ppb and that from changes in both photolysis rates and BVOC emissions

362   is about 3.5 ppb. In some regions, such as Midwestern, western Pennsylvania, and central New

363   York, the effect of BVOC emissions is negligible.

364

5.4. Cloud effects on ozone bias in VOC- and NO_X -limited regimes

366   In this section, we examine the effects of clouds on O_3 in VOC-limited and NO_X-limited regimes

367   in order to understand the reasons for a stronger O_3 response to cloud corrections in urban areas

368   than in the remote regions. Figure 7 shows how cloud corrections affect O_3 errors in different

369   regimes. Here, MDA8 O_3 is used to compute the model O_3 bias (simulation minus observation).

370   Figures 7a and 7b show the probability density functions of the model O_3 bias for the CNTR and

371   GOES simulations, respectively, at all ground sites experiencing considerably thick (COD > 20)

372   clouds. In this example, an EPA site is considered under cloudy sky conditions when hourly

373   COD greater than the chosen threshold (here, 20) is present at the site for at least 4 hours within

374   the 8-h time window in a given day. The decrease in the O_3 bias for VOC-limited regime is

375   significant, and the difference in median values between the two simulations is 5.2 ppb. The

376   decrease in O_3 bias for NO_X-limited regimes (2.7 ppb) is about 2 times smaller than that for

377   VOC-limited regime. An important result is that the frequency of very large biases (e.g., greater

378   than 20 ppb) is substantially reduced when cloud fields are corrected, especially for the VOC-

379   limited regime. This implies that more accurate cloud predictions ultimately improve the

380   accuracy of O_3 alert predictions, especially in polluted urban areas.

381   Figure 7c shows the change in median values of MDA8 O_3 bias for a range of COD thresholds.

382   We find that the O_3 bias increases with increasing cloudiness in the CNTR simulation. As

383   previously mentioned, the O_3 bias is generally larger for VOC-limited regimes than for NO_X-

384   limited regimes. When the radiation fields are corrected with satellite clouds, the model O_3 bias

385   is considerably reduced (but not zero). In addition, the O_3 bias in the GOES simulation does not

386   increase as much as that in the CNTR simulation when cloudiness increases. This implies that

387   there are other sources of O_3 biases in the GOES simulation, which are not likely associated with

388   cloudiness. The other errors sources can be precursor emissions, mixing/transport, and deposition.

389   Fig. 7d compares the median values of MDA8 O_3 bias between the two simulations (CNTR

390   minus GOES), and shows that the difference in MDA8 O_3 between the two simulations clearly

391   increases as the COD threshold increases and that the effect of cloud correction is larger in VOC-

392   limited than in NO_X-limited regimes. The reduced O_3 bias as a result of cloud corrections ranges

393   from 1 to 5 ppb depending on CODs and chemistry regimes. This represents up to ~40% of the

394   total O_3 bias under cloudy conditions in the current model version (e.g., 5.2 ppb of 12.6 ppb for

395   COD threshold of 20 in VOC-limited regimes). Note that the results for the sites in transitional

396   zone (the slope of $\Delta O_3/\Delta NO_y$ is 4–6) showed that the effects of cloud in the transitional zone are

397   intermediate; that is, larger than those for NO_X-limited regimes but smaller than those for VOC-

398   limited regimes (not shown).

399   We performed additional analysis by dividing VOC- and NO_X-limited sites into groups that have

400   similar ranges of peak MDA8 O_3 concentration during the period of June–September 2013 (Fig.

401   S3). All sites are grouped into bins with peak value of MDA8 O_3 ranging from larger than 75

402   ppb, 70–75 ppb, 65–70 ppb, 60–65 ppb, to smaller than 60 ppb. The maximum reduction in O_3

403   bias due to cloud corrections is obtained for the VOC-limited sites with peak MDA8 O_3 of 65–70

404   ppb and reaches ~8 ppb. The maximum reduction for NO_X-limited sites, on the other hand, is ~4

405   ppb and found for the sites with peak MDA8 O_3 of 70–75 ppb. Although the degree of the O_3

406   bias reduction varies somewhat among the bins for a given ozone regime, the effects of cloud

407   correction on O_3 bias reduction remain larger in VOC-limited regimes than NO_X-limited regimes.

408   We examine the O_3 bias over the southeast US where large overpredictions at the surface have

409   been reported (e.g., Travis et al. 2016) in the supplementary material. It is found that a

410   considerable portion of O_3 bias is attributable to inaccurate cloud predictions over the southeast

411   US, but the degree of the effects of clouds is smaller than that over CONUS as a whole (Fig. S4).

412   The maximum reduction in O_3 bias due to inaccurate cloud predictions is 4.5 ppb over the

413   southeast US and 5.3 ppb over CONUS. Still, large O_3 biases of ~11 ppb are present over the

414   southeast US (compared to those of 6–9 ppb over CONUS) even though the clouds and radiation

415   fields that are relevant to photochemistry are corrected. This result implies that errors resulting

416   from other processes exist and are responsible for the surface O_3 overpredictions over the

417   southeast US. More in-depth studies that find and quantify errors are therefore required to better

418   predict the O_3 over the southeast US as well as CONUS.

419

420   **5.5. Ozone formation sensitivity to changes in photolysis rates**

421   The difference in O_3 sensitivity to changes in photolysis rates (resulting from the presence of

422   clouds) in different regimes is determined by calculating $dln(O_3)/dln(JNO_2)$ ratios as in

423   Kleinman (1991). Table 3 lists those sensitivity coefficients of O_3 to JNO_2 and shows that O_3 is

424   more sensitive to JNO_2 in VOC-limited than in NO_X-limited regimes, being 1.69 times larger

425   under cloudy-sky conditions and by 1.65 times greater under clear-sky conditions. Similar

426   sensitivities were reported for OH by Berresheim et al. (2003) with the sensitivity of OH to JO^1D,

427     $dln(OH)/dln(JO^1D)$, of 0.8 at high NO_2 levels (~10 ppb) and 0.68 at low to moderate NO_2 levels

428   (~1 ppb). The corresponding sensitivities from our study are 1.1 for VOC-limited regimes and

429   0.66 for NO_X-limited regimes under clear-sky conditions. Similar results are also found for the

430   net chemical production of O_3 and OH concentration, revealing stronger responses to changes in

431   cloudiness in VOC-limited regimes than NO_X-limited regimes (Fig. 8). It is interesting to note

432   that OH and HO_2 have local maxima at CODs between 2 and 5. As shown in Ryu et al. (2017),

433   the enhancement of actinic flux at the surface due to optically thin clouds (CODs < 5) is

434   considerable for high-level clouds, i.e., cirrus. The local maxima, therefore, likely result from the

435   fact that the GOES clouds have the largest portion of cirrus for CODs of 2–5 as seen in Fig. 2b.

436   Figure 8 also shows that the variation (defined by 25 and 75 percentiles) of net chemical

437   production of O_3 with respect to COD is much larger in VOC-limited conditions. This result

438   suggests that predicting O_3 under cloudy conditions is likely more difficult in VOC-limited than

439   in NO_X-limited regimes. It is also noticeable that the HO_2 radical concentration remains

440   relatively high in NO_X-limited regimes even under cloudy conditions as compared to the VOC-

441   limited regimes. Note that the results of WRF-Chem here include the effects of both photolysis

442   rates and BVOC emissions.

443   A simplified box model (BOXMOX, Knote et al. (2015)) simulation using the same chemical

444   mechanism (MOZART-4) as WRF-Chem was performed to better understand O_3 sensitivity to

445   changing cloudiness in different chemistry regimes. The emission rates for VOC-limited (NO_X-

446   limited) regime are those of the Chicago urban (rural) area in the WRF-Chem simulation. The

447   initial conditions are taken from the CNTR simulation at 09 CST 7 July 2013 in the Chicago

448   suburban area for both regimes. Dry deposition is not considered. Photolysis rates for all species

449   that are photodissociable are varied from clear-sky to cloudy conditions with up to 80%

450   reduction. The 80% reduction roughly corresponds to COD of 35 (not shown). The box model is

451   integrated for 3 hours and photolysis rates are kept constant during the simulation (i.e., no

452   diurnal variations). The box model results are found to be consistent with the results from the

453   WRF-Chem simulations: the variations of O_3 and OH with respect to decreasing photolysis rates

454   are larger in VOC-limited regime than in NO_X-limited regime (Fig. S5, in the supplementary

455   material). Note that the net chemical production of O_3 obtained from the box model results also

456   shows a larger sensitivity to cloudiness in VOC-limited regimes than in NO_X-limited regimes,

457   which is similar to Figs. 8a and 8d (not shown). Figure 9 shows production and loss terms of

458   RO_X (= OH + HO_2 + RO_2) radicals with variations in photolysis rates for VOC-limited and NO_X-

459   limited regimes. In both regimes, the decreased sunlight due to clouds reduces OH formation by

460   photodissociation of O_3 (primary source of OH). The larger sensitivity of OH radicals to COD in

461   VOC-limited regimes as seen in Fig. 8 is associated with the loss of OH by the radical

462   termination reaction between OH and NO_2 under NO_X-rich conditions, which leads to the large

463   decrease in OH (Fig. 9a). On the other hand, in NO_X-limited regimes, the radical termination

464   reactions are the radical-radical reactions (Fig. 9b). In this regime, OH mainly reacts with VOCs

465   and propagates through radical cycles by producing HO_2/RO_2 radicals, rather than being

466   terminated by the reaction with NO_2. Given that the reaction between NO and HO_2 becomes the

467   largest source of OH budget (secondary source of OH) at an NO_X concentration of ~1 ppb

468   (Ehhalt and Rohrer, 2000; Eisele et al., 1997), OH can be relatively less sensitive to the changes

469   in radiation. Note that the mean daytime NO_X concentration over CONUS in NO_X-limited

470 regimes is 1.2 ppb and that in VOC-limited regimes is 6.7 ppb for this study period. Another

471 attribute is a greater contribution of H_2O_2 photodissociation to the production of RO_X in NO_X-

472 limited regimes than that of HNO_3, which is negligible. Unlike the radical terminated in VOC-

473 limited conditions, a non-negligible amount of terminated radicals can be recycled in the NO_X-

474 limited regime.

475

6. Sensitivity of cloud optical depth and O_3 to microphysics and convective schemes

478 It should be emphasized that our study was performed using a specific representation of the

479 cloud microphysics by Morrison et al. (2009) and cumulus parameterization (Grell and Devenyi,

480 2002). To test the robustness of our results with regard to the representation of clouds, another

481 microphysics scheme, Thompson scheme (Thompson et al., 2008), is employed for a 10-day (3

482 July–12 July 2013) sensitivity simulation. The COD comparison in Fig. S6 shows that with the

483 Thompson scheme the model predicts fewer clouds for all ranges of CODs as compared to

484 GOES retrievals, except for the very thin ones (COD < 1) in which the number of those clouds is

485 still overpredicted as seen in the simulation with Morrison scheme. Compared to the Morrison

486 scheme, the Thompson scheme produces significantly less high-level (cirrus) clouds. This is also

487 consistent with the findings of Cintineo et al. (2013). Despite this difference, the shape of the

488 COD distribution from the two microphysics schemes are rather similar to each other.

489 The MDA8 O_3 bias with the Thompson scheme is evaluated (Fig. S7), and compared to that of

490 the Morrison scheme for the same period. Under the conditions of COD greater than 20, for

491 example, the baseline simulation with the Thompson scheme (that uses model generated clouds)

492   shows that a median bias (14.79 ppb) is a bit smaller than that with the Morrison scheme (16.22

493   ppb) for that period in VOC-limited regimes. In the sensitivity simulation with the Thompson

494   scheme that uses GOES satellite clouds for photochemistry, the median bias is reduced by 5.45

495   ppb (~37%, Fig. S7a) in VOC-limited regimes and by 2.06 ppb (~20%, Fig. S7c) in NO_X-limited

496   regimes, which are consistent with the results of our base simulation. The degree of the effects of

497   cloud correction in the sensitivity simulations with the Thompson scheme, ranging from 0.5 to

498   5.5 ppb, is similar to that found in our base simulation with the Morrison scheme. Therefore, the

499   general conclusions remain the same: i.e., errors in O_3 predictions resulting from errors in cloud

500   predictions are considerable (up to ~5 ppb on average) and the effects of cloud corrections are

501   larger in VOC-limited regimes than in NO_X-limited regimes.

502   To estimate the sensitivity of our results to cumulus parameterization schemes, sensitivity

503   simulations with the Grell-Freitas scheme (Grell and Freitas, 2014) are performed. As done for

504   microphysics scheme, a period of 10 days (3–12 July 2013) was considered. In Fig. S8, the

505   histograms of cloud optical depths obtained for the 10-day period from Grell-Freitas scheme and

506   from Grell-3D scheme show that the distributions of cloud optical depths are in general similar

507   to each other. The Grell-Freitas scheme tends to produce fewer clouds with small or moderate

508   cloud optical depths (Fig. S8). As shown in Fig. S9, the degree of cloud correction in reducing

509   O_3 bias is larger in VOC-limited regimes than in NO_X-limited regimes in the simulation with

510   Grell-Freitas scheme, and thus the conclusions originally drawn remain unchanged.

511

7. Conclusions and discussion

We performed quantitative analyses of the WRF-Chem model meso-scale (12 km) simulations to determine how much errors in cloud predictions contribute to errors in surface O_3 predictions during summertime over CONUS. Clouds were generated using the Morrison microphysics and Grell 3D cumulus parameterization schemes. It is found that the WRF-Chem model is able to generate roughly 55% of the clouds in the right locations by comparing to satellite clouds. A quantitative comparison of COD shows that the WRF-Chem model predicts too many thin cirrus clouds with CODs less than 1, and also considerably underpredicts the optical depths for a majority of cloud systems.

The errors in cloud predictions can lead to large hourly O_3 biases of up to 60 ppb, for example, for specific cases in which the model misses deep convective clouds that are present in reality. On average, the errors in MDA8 O_3 of 1–5 ppb are found to be attributable to errors in cloud predictions under cloudy sky conditions. We quantify separately the contribution of changes in photolysis rates and emissions of light-dependent BVOCs to cloud-related errors in surface O_3. The contribution of photolysis rates to surface O_3 is larger (~80% on average) than that of BVOC emissions. The contribution of BVOC emissions to O_3 can become important (~40%) in the VOC-limited regimes where BVOC emissions are large (i.e., cities of the southeast US).

The effects of cloud corrections are more impactful in VOC-limited (or high-NO_X) than in NO_X-limited (or low-NO_X) regimes. The sensitivity of O_3 with respect to COD is about 2 times larger in VOC-limited than in NO_X-limited regimes. This finding is consistent with the box modeling results that were performed for typical urban/rural conditions under varying photolysis rates. The production of radicals (OH, HO_2, and RO_2) decreases with decreasing photolysis rates in the presence of clouds. The primary reason for the larger sensitivity of O_3 formation to clouds in

535 VOC-limited regimes is that the loss of OH is much stronger in VOC-limited regimes due to the

536 reaction with NO_2. Thus, OH cannot readily propagate through the radical cycles. In NO_X-

537 limited regimes, the radicals terminated from the radical cycles are mostly HO_2 and RO_2 rather

538 than OH. Thus, OH can remain in the cycles and continue to produce HO_2 and RO_2 by reacting

539 with VOCs before termination. The interconversion of HO_2 to OH is the dominant process in

540 NO_X-limited regimes, and therefore OH and O_3 formations are less sensitive to changes in

541 radiation.

542 We showed that considerable reduction in O_3 bias is achieved by correcting cloud-related

543 radiation fields; however, O_3 is still overpredicted by the WRF-Chem model. The remaining bias

544 likely results from other processes involved in the O_3 lifecycle such as precursor emissions from

545 both anthropogenic and biogenic sources, transport, turbulent mixing, and dry deposition, which

546 quantitative assessment is beyond the scope of this study.

547 One should keep in mind that the quantitative estimate of the O_3 bias related to the cloud effects

548 on radiation as reported in this study could be sensitive to several factors. In particular, this study

549 is based on a particular configuration of the WRF-Chem model with regard to the radiation,

550 microphysics, cumulus, boundary layer parameterization and the chemistry scheme. We have

551 tested the sensitivity of our results to the choice of microphysics and cumulus parameterization

552 schemes, and have shown that MDA8 O_3 biases are reduced by up to ~5 ppb with the satellite

553 cloud corrections in the simulations with the different microphysics and cumulus

554 parameterization schemes, which is consistent with the results found in our base simulations.

555 This study suggests that accurate cloud predictions through data assimilation or cloud mask

556 corrections with near-real time satellite cloud data would improve the accuracy of O_3 predictions

557   and that the benefit is expected to be greater in VOC-limited than in NO_X-limited regimes. It

558   should be noted that our estimates are based on WRF-Chem simulations that use initial and

559   boundary conditions from meteorological analysis data, which is an improved estimate of the

560   meteorological state compared to forecast data, and thus the reduction of errors in O_3 predictions

561   could be even greater in a forecasting setting. From the perspective of O_3 forecast, our study

562   indicates that there is a need for an enhanced understanding of the evolution of errors in O_3

563   forecasts associated with errors in cloud forecasts, and for optimizing the use of meteorological

564   forecasts to allow more accurate near-term O_3 predictions. The present study corrects cloud

565   fields in WRF using satellite clouds only for radiation that is relevant to photochemistry, and

566   those cloud corrections do not affect other meteorological variables such as surface temperature,

567   wind, humidity, boundary layer height, etc. In a future study, we plan to examine the effects of

568   satellite cloud assimilation on near-term O_3 forecasts using enhanced forecasts such as the Rapid

569   Refresh products from NOAA (Benjamin et al., 2016) that take into account cloud data

570   assimilation to derive meteorology. The Rapid Refresh uses satellite cloud products as well as

571   cloud observations from the ground and considers the thermodynamic balance between

572   temperature and humidity due to the presence of clouds. Thus, this will allow investigating the

573   effects of cloud assimilation on O_3 forecasts not only through changes in radiation for

574   photochemistry but also through changes in meteorological variables.

575

576   **Acknowledgments**

577   We acknowledge Samuel Hall and Kirk Ullmann for providing actinic flux data that are used for

578   supplementary analysis, George Grell and Geoff Tyndall for helpful discussions. This study is

579   supported from NASA-ROSES grant NNX15AE38G. P. Minnis was supported by the NASA

580   Modeling, Analysis, and Prediction Program. The National Center for Atmospheric Research is

581   sponsored by the National Science Foundation. We would like to acknowledge high-performance

582   computing support from Cheyenne (doi:10.5065/D6RX99HX) provided by NCAR's

583   Computational and Information Systems Laboratory, sponsored by the National Science

584   Foundation. The GOES cloud retrievals are available at https://satcorps.larc.nasa.gov. The EPA

585   ozone data can be downloaded at

586   https://aqsdr1.epa.gov/aqsweb/aqstmp/airdata/download_files.html.

587

588

589

590

591

592

593

594

595

596

597

599   **Reference**

600   Bei, N., Lei, W., Zavala, M. and Molina, L. T.: Ozone predictabilities due to meteorological

601   uncertainties in the Mexico City basin using ensemble forecasts, Atmos Chem Phys, 10(13),

602   6295–6309, doi:10.5194/acp-10-6295-2010, 2010.

603   Benjamin, S. G., Weygandt, S. S., Brown, J. M., Hu, M., Alexander, C. R., Smirnova, T. G.,

604   Olson, J. B., James, E. P., Dowell, D. C., Grell, G. A., Lin, H., Peckham, S. E., Smith, T. L.,

605   Moninger, W. R., Kenyon, J. S. and Manikin, G. S.: A North American Hourly Assimilation and

606   Model Forecast Cycle: The Rapid Refresh, Mon. Wea. Rev., 144(4), 1669–1694,

607   doi:10.1175/MWR-D-15-0242.1, 2015.

608   Berresheim, H., Plass-Dülmer, C., Elste, T., Mihalopoulos, N. and Rohrer, F.: OH in the coastal

609   boundary layer of Crete during MINOS: Measurements and relationship with ozone photolysis,

610   Atmos Chem Phys, 3(3), 639–649, doi:10.5194/acp-3-639-2003, 2003.

611   Briegleb, B. P.: Delta-Eddington approximation for solar radiation in the NCAR community

612   climate model, J. Geophys. Res. Atmospheres, 97(D7), 7603–7612, doi:10.1029/92JD00291,

613   1992.

614   Brioude, J., Angevine, W. M., Ahmadov, R., Kim, S.-W., Evan, S., McKeen, S. A., Hsie, E.-Y.,

615   Frost, G. J., Neuman, J. A., Pollack, I. B., Peischl, J., Ryerson, T. B., Holloway, J., Brown, S. S.,

616   Nowak, J. B., Roberts, J. M., Wofsy, S. C., Santoni, G. W., Oda, T. and Trainer, M.: Top-down

617   estimate of surface flux in the Los Angeles Basin using a mesoscale inverse modeling technique:

618   assessing anthropogenic emissions of CO, NOx and CO2 and their impacts, Atmos Chem Phys,

619   13(7), 3661–3677, doi:10.5194/acp-13-3661-2013, 2013.

620 Brown-Steiner, B., Hess, P. G. and Lin, M. Y.: On the capabilities and limitations of GCCM

621 simulations of summertime regional air quality: A diagnostic analysis of ozone and temperature

622 simulations in the US using CESM CAM-Chem, Atmos. Environ., 101, 134–148,

623 doi:10.1016/j.atmosenv.2014.11.001, 2015.

624 Campbell, P., Zhang, Y., Yahya, K., Wang, K., Hogrefe, C., Pouliot, G., Knote, C., Hodzic, A.,

625 San Jose, R., Perez, J. L., Jimenez Guerrero, P., Baro, R. and Makar, P.: A multi-model

626 assessment for the 2006 and 2010 simulations under the Air Quality Model Evaluation

627 International Initiative (AQMEII) phase 2 over North America: Part I. Indicators of the

628 sensitivity of O3 and PM2.5 formation regimes, Atmos. Environ., 115, 569–586,

629 doi:10.1016/j.atmosenv.2014.12.026, 2015.

630 Carter, W. P. L.: Development of the SAPRC-07 chemical mechanism, Atmos. Environ., 44(40),

631 5324–5335, doi:10.1016/j.atmosenv.2010.01.026, 2010.

632 Chang, J. S., Brost, R. A., Isaksen, I. S. A., Madronich, S., Middleton, P., Stockwell, W. R. and

633 Walcek, C. J.: A three-dimensional Eulerian acid deposition model: Physical concepts and

634 formulation, J. Geophys. Res. Atmospheres, 92(D12), 14681–14700,

635 doi:10.1029/JD092iD12p14681, 1987.

636 Chen, F. and Dudhia, J.: Coupling an Advanced Land Surface–Hydrology Model with the Penn

637 State–NCAR MM5 Modeling System. Part I: Model Implementation and Sensitivity, Mon.

638 Weather Rev., 129(4), 569–585, doi:10.1175/1520-0493(2001)129<0569:CAALSH>2.0.CO;2,

639 2001.

640   Cintineo, R., Otkin, J. A., Xue, M. and Kong, F.: Evaluating the Performance of Planetary

641   Boundary Layer and Cloud Microphysical Parameterization Schemes in Convection-Permitting

642   Ensemble Forecasts Using Synthetic GOES-13 Satellite Observations, Mon. Weather Rev.,

643   142(1), 163–182, doi:10.1175/MWR-D-13-00143.1, 2013.

644   Cleary, P. A., Fuhrman, N., Schulz, L., Schafer, J., Fillingham, J., Bootsma, H., McQueen, J.,

645   Tang, Y., Langel, T., McKeen, S., Williams, E. J., and Brown, S. S.: Ozone distributions over

646   southern Lake Michigan: comparisons between ferry-based observations, shoreline-based DOAS

647   observations   and   model   forecasts,   Atmos.   Chem.   Phys.,   15,   5109-5122,

648   https://doi.org/10.5194/acp-15-5109-2015, 2015.

649   Dabberdt, W. F., Carroll, M. A., Baumgardner, D., Carmichael, G., Cohen, R., Dye, T., Ellis, J.,

650   Grell, G., Grimmond, S., Hanna, S., Irwin, J., Lamb, B., Madronich, S., McQueen, J., Meagher,

651   J., Odman, T., Pleim, J., Schmid, H. P. and Westphal, D. L.: Meteorological Research Needs for

652   Improved Air Quality Forecasting: Report of the 11th Prospectus Development Team of the U.S.

653   Weather Research Program*, Bull. Am. Meteorol. Soc., 85(4), 563–586, doi:10.1175/BAMS-85-

654   4-563, 2004.

655   Ehhalt, D. H. and Rohrer, F.: Dependence of the OH concentration on solar UV, J. Geophys. Res.

656   Atmospheres, 105(D3), 3565–3571, doi:10.1029/1999JD901070, 2000.

657   Eisele, F. L., Mount, G. H., Tanner, D., Jefferson, A., Shetter, R., Harder, J. W. and Williams, E.

658   J.: Understanding the production and interconversion of the hydroxyl radical during the

659   Tropospheric OH Photochemistry Experiment, J. Geophys. Res. Atmospheres, 102(D5), 6457–

660   6465, doi:10.1029/96JD02207, 1997.

661 Fiore, A. M., Dentener, F. J., Wild, O., Cuvelier, C., Schultz, M. G., Hess, P., Textor, C., Schulz,

662 M., Doherty, R. M., Horowitz, L. W., MacKenzie, I. A., Sanderson, M. G., Shindell, D. T.,

663 Stevenson, D. S., Szopa, S., Van Dingenen, R., Zeng, G., Atherton, C., Bergmann, D., Bey, I.,

664 Carmichael, G., Collins, W. J., Duncan, B. N., Faluvegi, G., Folberth, G., Gauss, M., Gong, S.,

665 Hauglustaine, D., Holloway, T., Isaksen, I. S. A., Jacob, D. J., Jonson, J. E., Kaminski, J. W.,

666 Keating, T. J., Lupu, A., Marmer, E., Montanaro, V., Park, R. J., Pitari, G., Pringle, K. J., Pyle, J.

667 A., Schroeder, S., Vivanco, M. G., Wind, P., Wojcik, G., Wu, S. and Zuber, A.: Multimodel

668 estimates of intercontinental source-receptor relationships for ozone pollution, J. Geophys. Res.

669 Atmospheres, 114(D4), D04301, doi:10.1029/2008JD010816, 2009.

670 Grell, G. A. and Devenyi, D.: A generalized approach to parameterizing convection combining

671 ensemble and data assimilation techniques, Geophys. Res. Lett., 29(14), 38–1,

672 doi:10.1029/2002GL015311, 2002.

673 Grell, G. A. and Freitas, S. R.: A scale and aerosol aware stochastic convective parameterization

674 for weather and air quality modeling, Atmos. Chem. Phys., 14, 5233–5250,

675 https://doi.org/10.5194/acp-14-5233-2014, 2014.

676 Guenther, A., Karl, T., Harley, P., Wiedinmyer, C., Palmer, P. I. and Geron, C.: Estimates of

677 global terrestrial isoprene emissions using MEGAN (Model of Emissions of Gases and Aerosols

678 from Nature), Atmos Chem Phys, 6(11), 3181–3210, doi:10.5194/acp-6-3181-2006, 2006.

679 Hodzic, A., Ryu, Y.-H., Madronich, S., Walters, S.: Modeling and evaluation of actinic fluxes

680 and photolysis rates in WRF-Chem, In preparation.

681   Iacono, M. J., Delamere, J. S., Mlawer, E. J., Shephard, M. W., Clough, S. A. and Collins, W. D.:

682   Radiative forcing by long-lived greenhouse gases: Calculations with the AER radiative transfer

683   models, J. Geophys. Res. Atmospheres, 113(D13), D13103, doi:10.1029/2008JD009944, 2008.

684   Im, U., Bianconi, R., Solazzo, E., Kioutsioukis, I., Badia, A., Balzarini, A., Baró, R., Bellasio, R.,

685   Brunner, D., Chemel, C., Curci, G., Flemming, J., Forkel, R., Giordano, L., Jiménez-Guerrero, P.,

686   Hirtl, M., Hodzic, A., Honzak, L., Jorba, O., Knote, C., Kuenen, J. J. P., Makar, P. A., Manders-

687   Groot, A., Neal, L., Pérez, J. L., Pirovano, G., Pouliot, G., San Jose, R., Savage, N., Schroder,

688   W., Sokhi, R. S., Syrakov, D., Torian, A., Tuccella, P., Werhahn, J., Wolke, R., Yahya, K.,

689   Zabkar, R., Zhang, Y., Zhang, J., Hogrefe, C. and Galmarini, S.: Evaluation of operational on-

690   line-coupled regional air quality models over Europe and North America in the context of

691   AQMEII   phase   2.   Part   I: Ozone,   Atmos.   Environ.,   115,   404–420,

692   doi:10.1016/j.atmosenv.2014.09.042, 2015.

693   Kleinman, L. I.: Seasonal dependence of boundary layer peroxide concentration: The low and

694   high NO x   regimes, J. Geophys. Res. Atmospheres, 96(D11), 20721–20733,

695   doi:10.1029/91JD02040, 1991.

696   Knote, C., Hodzic, A., Jimenez, J. L., Volkamer, R., Orlando, J. J., Baidar, S., Brioude, J., Fast,

697   J., Gentner, D. R., Goldstein, A. H., Hayes, P. L., Knighton, W. B., Oetjen, H., Setyan, A., Stark,

698   H., Thalman, R., Tyndall, G., Washenfelder, R., Waxman, E. and Zhang, Q.: Simulation of semi-

699   explicit mechanisms of SOA formation from glyoxal in aerosol in a 3-D model, Atmos Chem

700   Phys, 14(12), 6213–6239, doi:10.5194/acp-14-6213-2014, 2014.

701   Knote, C., Tuccella, P., Curci, G., Emmons, L., Orlando, J. J., Madronich, S., Baró, R., Jiménez-

702   Guerrero, P., Luecken, D., Hogrefe, C., Forkel, R., Werhahn, J., Hirtl, M., Pérez, J. L., San José,

R., Giordano, L., Brunner, D., Yahya, K. and Zhang, Y.: Influence of the choice of gas-phase mechanism on predictions of key gaseous pollutants during the AQMEII phase-2 intercomparison, Atmos. Environ., 115, 553–568, doi:10.1016/j.atmosenv.2014.11.066, 2015.

Lin, M., Horowitz, L. W., Payton, R., Fiore, A. M. and Tonnesen, G.: US surface ozone trends and extremes from 1980 to 2014: quantifying the roles of rising Asian emissions, domestic controls, wildfires, and climate, Atmos Chem Phys, 17(4), 2943–2970, doi:10.5194/acp-17-2943-2017, 2017.

Mayer, B., Fischer, C. A. and Madronich, S.: Estimation of surface actinic flux from satellite (TOMS) ozone and cloud reflectivity measurements, Geophys. Res. Lett., 25(23), 4321–4324, doi:10.1029/1998GL900140, 1998.

Minnis, P., Nguyen, L., Palikonda, R., Heck, P. W. Spangenberg, D. A., Doelling, D. R., Ayers, J. K., Smith, W. L., Jr., Khaiyer, M. M., Trepte, Q. Z., Avey, L. A., Chang, F.-L., Yost, C. R., Chee, T. L., and Sun-Mack, S.: Near-real time cloud retrievals from operational and research meteorological satellites, Proc. SPIE Remote Sens. Clouds Atmos. XIII, 7107-2, 8 pp., ISBN: 9780819473387, 2008.

Minnis, P., Sun-Mack, S., Trepte, Q. Z., Chang, F.-L., Heck, P. W., Chen, Y., Yi, Y., Arduini, R. F., Ayers, K., Bedka, K., Bedka, S., Brown, R., Gibson, S., Heckert, E., Hong, G., Jin, Z. Palikonda, R. Smith, R. Smith, W. l., Jr., Spangenberg, D. A. Yang, P., Yost, C. R., and Xie, Y.: CERES Edition 3 cloud retrievals. *AMS 13th Conf. Atmos. Rad.*, Portland, OR, June 27 – July 2, 5.4, 7 pp., 2010.

Minnis, P., Sun-Mack, S., Young, D. F., Heck, P. W., Garber, D. P., Chen, Y., Spangenberg, D. A., Arduini, R. F., Trepte, Q. Z., Smith, W. L., Ayers, J. K., Gibson, S. C., Miller, W. F., Hong,

725 G., Chakrapani, V., Takano, Y., Liou, K. N., Xie, Y. and Yang, P.: CERES Edition-2 Cloud

726 Property Retrievals Using TRMM VIRS and Terra and Aqua MODIS Data #x2014;Part I:

727 Algorithms, IEEE Trans. Geosci. Remote Sens., 49(11), 4374–4400,

728 doi:10.1109/TGRS.2011.2144601, 2011.

729 Minnis, P., Bedka, K., Q. Trepte, Q., Yost, C. R., Bedka, S. T., Scarino, B., Khlopenkov, K., and

730 Khaiyer, M. M., 2016: A consistent long-term cloud and clear-sky radiation property dataset

731 from the Advanced Very High Resolution Radiometer (AVHRR), Climate Algorithm

732 Theoretical Basis Document (C-ATBD), CDRP-ATBD-0826 Rev 1 AVHRR Cloud Properties -

733 NASA, NOAA CDR Program, 19 September, 159 pp.,DOI:10.789/V5HT2M8T, 2016.

734 Morrison, H., Thompson, G. and Tatarskii, V.: Impact of Cloud Microphysics on the

735 Development of Trailing Stratiform Precipitation in a Simulated Squall Line: Comparison of

736 One- and Two-Moment Schemes, Mon. Weather Rev., 137(3), 991–1007,

737 doi:10.1175/2008MWR2556.1, 2009.

738 Nakanishi, M. and Niino, H.: An Improved Mellor–Yamada Level-3 Model: Its Numerical

739 Stability and Application to a Regional Prediction of Advection Fog, Bound.-Layer Meteorol.,

740 119(2), 397–407, doi:10.1007/s10546-005-9030-8, 2006.

741 Pour-Biazar, A., McNider, R. T., Roselle, S. J., Suggs, R., Jedlovec, G., Byun, D. W., Kim, S.,

742 Lin, C. J., Ho, T. C., Haines, S., Dornblaser, B. and Cameron, R.: Correcting photolysis rates on

743 the basis of satellite observed clouds, J. Geophys. Res. Atmospheres, 112(D10), D10302,

744 doi:10.1029/2006JD007422, 2007.

745   Rossow, W. B. and Schiffer, R. A.: Advances in Understanding Clouds from ISCCP, Bull. Am.

746   Meteorol. Soc., 80(11), 2261–2287, doi:10.1175/1520-0477(1999)080<2261:AIUCFI>2.0.CO;2,

747   1999.

748   Ryu, Y.-H., Hodzic, A., Descombes, G., Hall, S., Minnis, P., Spangenberg, D., Ullmann, K. and

749   Madronich, S.: Improved modeling of cloudy-sky actinic flux using satellite cloud retrievals,

750   Geophys. Res. Lett., 44(3), 2016GL071892, doi:10.1002/2016GL071892, 2017.

751   Sarwar, G., Godowitch, J., Henderson, B. H., Fahey, K., Pouliot, G., Hutzell, W. T., Mathur, R.,

752   Kang, D., Goliff, W. S. and Stockwell, W. R.: A comparison of atmospheric composition using

753   the Carbon Bond and Regional Atmospheric Chemistry Mechanisms, Atmos Chem Phys, 13(19),

754   9695–9712, doi:10.5194/acp-13-9695-2013, 2013.

755   Sillman, S. and He, D.: Some theoretical results concerning O3-NOx-VOC chemistry and NOx-

756   VOC indicators, J. Geophys. Res. Atmospheres, 107(D22), 4659, doi:10.1029/2001JD001123,

757   2002.

758   Sun-Mack, S., Minnis, P., Chen, Y., Kato, S., Yi, Y., Gibson, S. C., Heck, P. W. and Winker, D.

759   M.: Regional Apparent Boundary Layer Lapse Rates Determined from CALIPSO and MODIS

760   Data for Cloud-Height Determination, J. Appl. Meteorol. Climatol., 53(4), 990–1011,

761   doi:10.1175/JAMC-D-13-081.1, 2014.

762   Tang, W., Cohan, D. S., Pour-Biazar, A., Lamsal, L. N., White, A. T., Xiao, X., Zhou, W.,

763   Henderson, B. H. and Lash, B. F.: Influence of satellite-derived photolysis rates and NOx

764   emissions on Texas ozone modeling, Atmos Chem Phys, 15(4), 1601–1619, doi:10.5194/acp-15-

765   1601-2015, 2015.

766 Tang, Y., Lee, P., Tsidulko, M., Huang, H.-C., McQueen, J. T., DiMego, G. J., Emmons, L. K.,

767 Pierce, R. B., Thompson, A. M., Lin, H.-M., Kang, D., Tong, D., Yu, S., Mathur, R., Pleim, J. E.,

768 Otte, T. L., Pouliot, G., Young, J. O., Schere, K. L., Davidson, P. M. and Stajner, I.: The impact

769 of chemical lateral boundary conditions on CMAQ predictions of tropospheric ozone over the

770 continental United States, Environ. Fluid Mech., 9(1), 43–58, doi:10.1007/s10652-008-9092-5,

771 2009.

772 Thiel, S., Ammannato, L., Bais, A., Bandy, B., Blumthaler, M., Bohn, B., Engelsen, O., Gobbi,

773 G. P., Gröbner, J., Jäkel, E., Junkermann, W., Kazadzis, S., Kift, R., Kjeldstad, B., Kouremeti, N.,

774 Kylling, A., Mayer, B., Monks, P. S., Reeves, C. E., Schallhart, B., Scheirer, R., Schmidt, S.,

775 Schmitt, R., Schreder, J., Silbernagl, R., Topaloglou, C., Thorseth, T. M., Webb, A. R.,

776 Wendisch, M. and Werle, P.: Influence of clouds on the spectral actinic flux density in the lower

777 troposphere (INSPECTRO): overview of the field campaigns, Atmos Chem Phys, 8(6), 1789–

778 1812, doi:10.5194/acp-8-1789-2008, 2008.

779 Thompson, G., Field, P. R., Rasmussen, R. M. and Hall, W. D.: Explicit Forecasts of Winter

780 Precipitation Using an Improved Bulk Microphysics Scheme. Part II: Implementation of a New

781 Snow Parameterization, Mon. Weather Rev., 136(12), 5095–5115,

782 doi:10.1175/2008MWR2387.1, 2008.

783 Toon, O. B., Maring, H., Dibb, J., Ferrare, R., Jacob, D. J., Jensen, E. J., Luo, Z. J., Mace, G. G.,

784 Pan, L. L., Pfister, L., Rosenlof, K. H., Redemann, J., Reid, J. S., Singh, H. B., Thompson, A. M.,

785 Yokelson, R., Minnis, P., Chen, G., Jucks, K. W. and Pszenny, A.: Planning, implementation,

786 and scientific goals of the Studies of Emissions and Atmospheric Composition, Clouds and

Climate Coupling by Regional Surveys (SEAC4RS) field mission, J. Geophys. Res. Atmospheres, 121(9), 2015JD024297, doi:10.1002/2015JD024297, 2016.

Travis, K. R., Jacob, D. J., Fisher, J. A., Kim, P. S., Marais, E. A., Zhu, L., Yu, K., Miller, C. C., Yantosca, R. M., Sulprizio, M. P., Thompson, A. M., Wennberg, P. O., Crounse, J. D., St. Clair, J. M., Cohen, R. C., Laughner, J. L., Dibb, J. E., Hall, S. R., Ullmann, K., Wolfe, G. M., Pollack, I. B., Peischl, J., Neuman, J. A. and Zhou, X.: Why do models overestimate surface ozone in the Southeast United States?, Atmos Chem Phys, 16(21), 13561–13577, doi:10.5194/acp-16-13561-2016, 2016.

Wiedinmyer, C., Akagi, S. K., Yokelson, R. J., Emmons, L. K., Al-Saadi, J. A., Orlando, J. J. and Soja, A. J.: The Fire INventory from NCAR (FINN): a high resolution global model to estimate the emissions from open burning, Geosci Model Dev, 4(3), 625–641, doi:10.5194/gmd-4-625-2011, 2011.

Yang, P., Hong, G., Kattawar, G. W., Minnis, P. and Hu, Y.: Uncertainties Associated With the Surface Texture of Ice Particles in Satellite-Based Retrieval of Cirrus Clouds: Part II #x2014;Effect of Particle Surface Roughness on Retrieved Cloud Optical Thickness and Effective Particle Size, IEEE Trans. Geosci. Remote Sens., 46(7), 1948–1957, doi:10.1109/TGRS.2008.916472, 2008.

Zhang, F., Bei, N., Nielsen-Gammon, J. W., Li, G., Zhang, R., Stuart, A. and Aksoy, A.: Impacts of meteorological uncertainties on ozone pollution predictability estimated through meteorological and photochemical ensemble forecasts, J. Geophys. Res. Atmospheres, 112(D4), D04304, doi:10.1029/2006JD007429, 2007.

808   Zhang, Y., Bocquet, M., Mallet, V., Seigneur, C. and Baklanov, A.: Real-time air quality

809   forecasting, part II: State of the science, current research needs, and future prospects, Atmos.

810   Environ., 60, 656–676, doi:10.1016/j.atmosenv.2012.02.041, 2012.

811

812

813

814

815

816

817

818

819

820

821

822

823

824

825

826

827

828

829

830

831   Table 1. Description of WRF-Chem simulations.

	Photolysis rates	PAR	Analysis Period
CNTR	WRF clouds	WRF clouds	06 UTC 11 June–12 UTC 1 October
GOES	GOES clouds	GOES clouds	06 UTC 11 June–12 UTC 1 October
EMIS_BVOC	GOES clouds	WRF clouds	06 UTC 3 July–12 UTC 13 July

832

833

834

835

836

837

838

839

840

841

842

843

844

845

846   Table 2. Contingency table for WRF simulation and GOES satellite clouds. The number of data

847   for each category is normalized by the total number of data.

		GOES Satellite	
		Cloudy	Clear
WRF simulation	Cloudy	A (hit) 24.8%	B (false alarm) 10.4%
	Clear	C (miss) 19.8%	D (correct negative) 44.9%

848

849

850

851

852

853

854

855

856

857

858

859   Table 3. Sensitivity coefficient of O_3 to JNO_2, i.e., $dln(O_3)/dln(JNO_2)$. The values of

860    $dln(O_3)/dln(JNO_2)$ for the period of 09–13 LST are averages over only CONUS EPA stations

861   that have monotonically increasing O_3 concentrations with time.

	Cloudy sky ($5 < COD < 20$)	Clear sky
VOC-limited	0.59	1.27
NO_X-limited	0.35	0.77

862

863

864

865

866

867

868

869

870

871

872

873

874
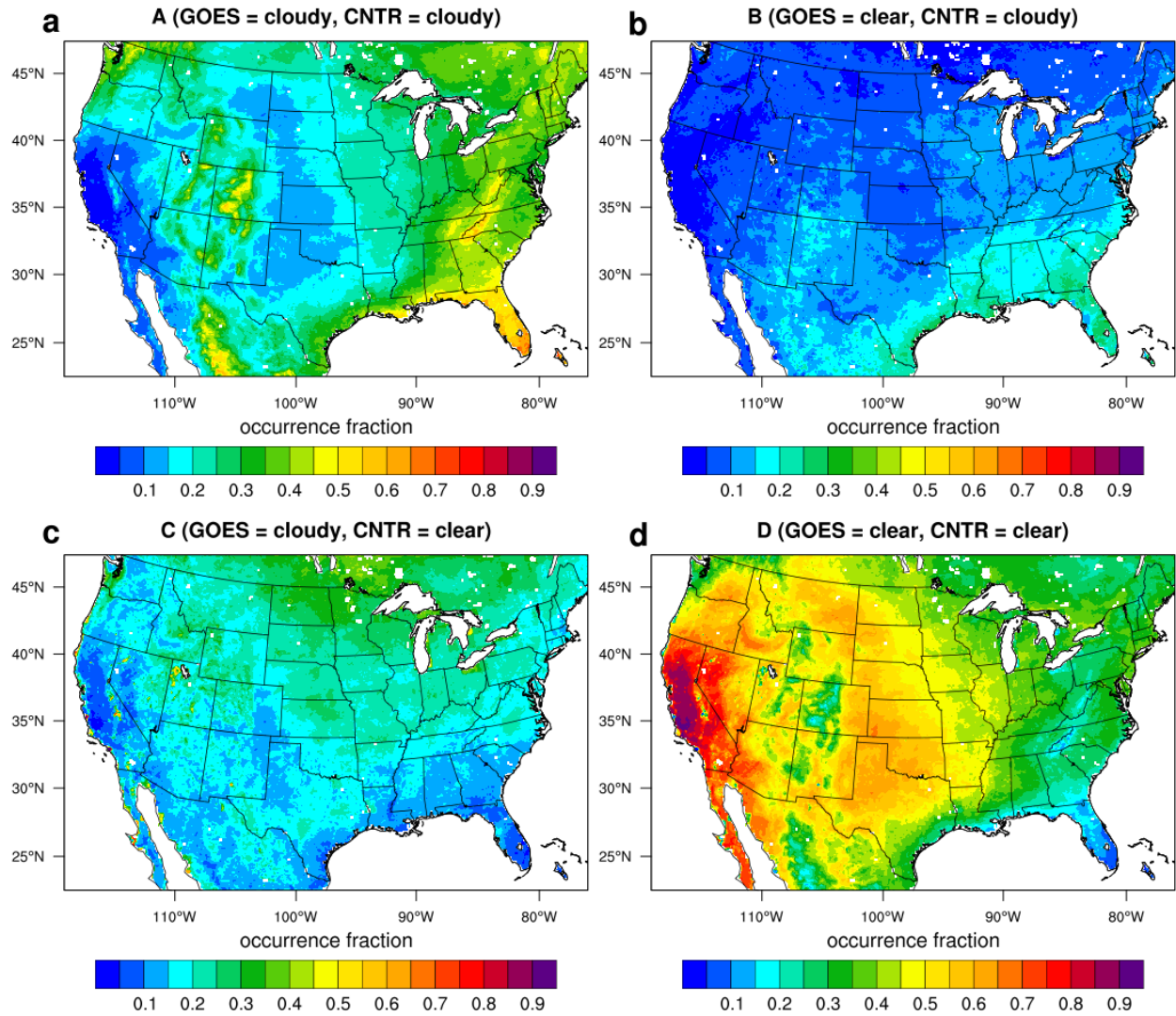
Fig. 1. Spatial distribution of each contingency category (see Table 2) between the WRF-generated clouds (CNTR simulation) and SatCORPS GOES retrievals averaged over the whole study period.

882
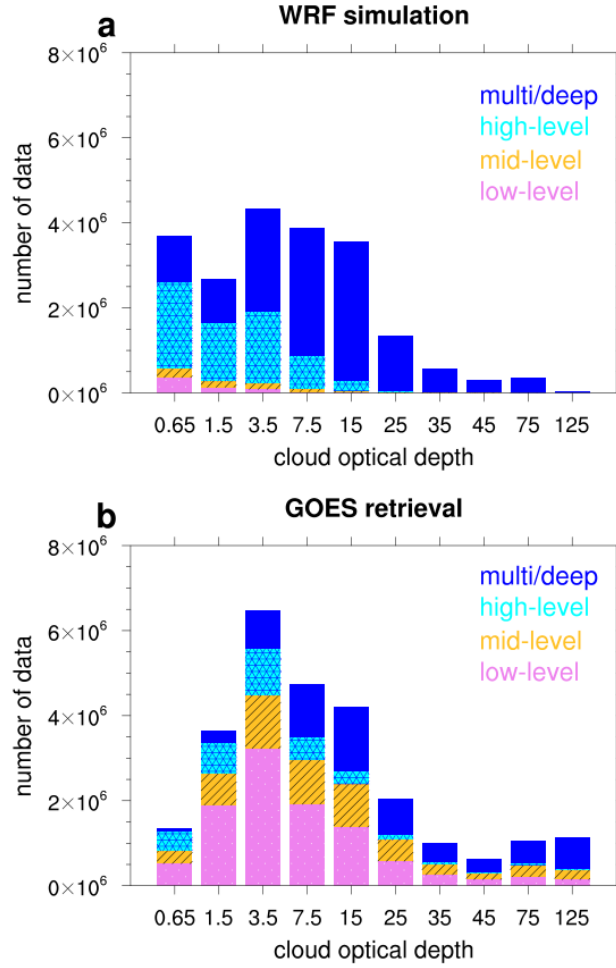
Fig. 2. Histogram of hourly cloud optical depth (COD) during the daytime (16–23 UTC) over
CONUS (land only) from the (a) WRF simulation (with the Morrison microphysics and the Grell
3-D schemes) and (b) GOES satellite retrievals. CODs on the *x*-axis represent the mean values of
the bins that are 0.3–1, 1–2, 2–5, 5–10, 10–20, 20–30, 30–40, 40–50, 50–100, and 100–150. For
a fair comparison, the multi-layered WRF clouds are not resolved into cloud layers as this
layering cannot be resolved by the satellite.

889

890

891
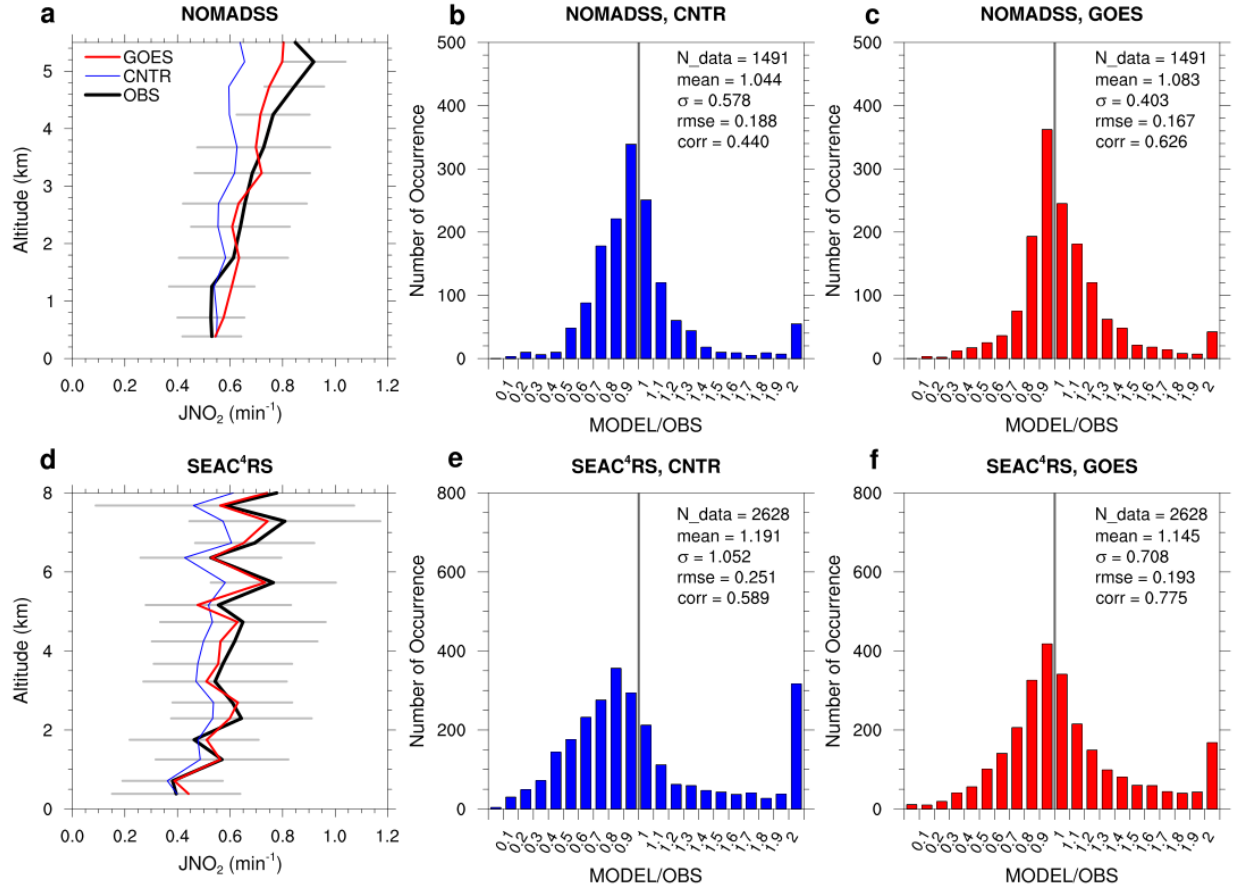
Fig. 3. Model evaluation with 16 NOMADSS flights (top row) and with 21 SEAC[4]RS flights
(bottom row). Note that only cloudy skies are considered. The comparison is performed for the
averaged vertical profiles of JNO_2 for the (a) NOMADSS and (d) SEAC[4]RS. The gray horizontal
lines indicate the standard deviations from the observations. Histogram of ratio of JNO_2
simulated by the model to JNO_2 observed (b) in the CNTR simulation and (c) in the GOES
simulation for the NOMADSS. (e and f) are the same as (b and c), respectively, but for the
SEAC[4]RS.

899

900

901
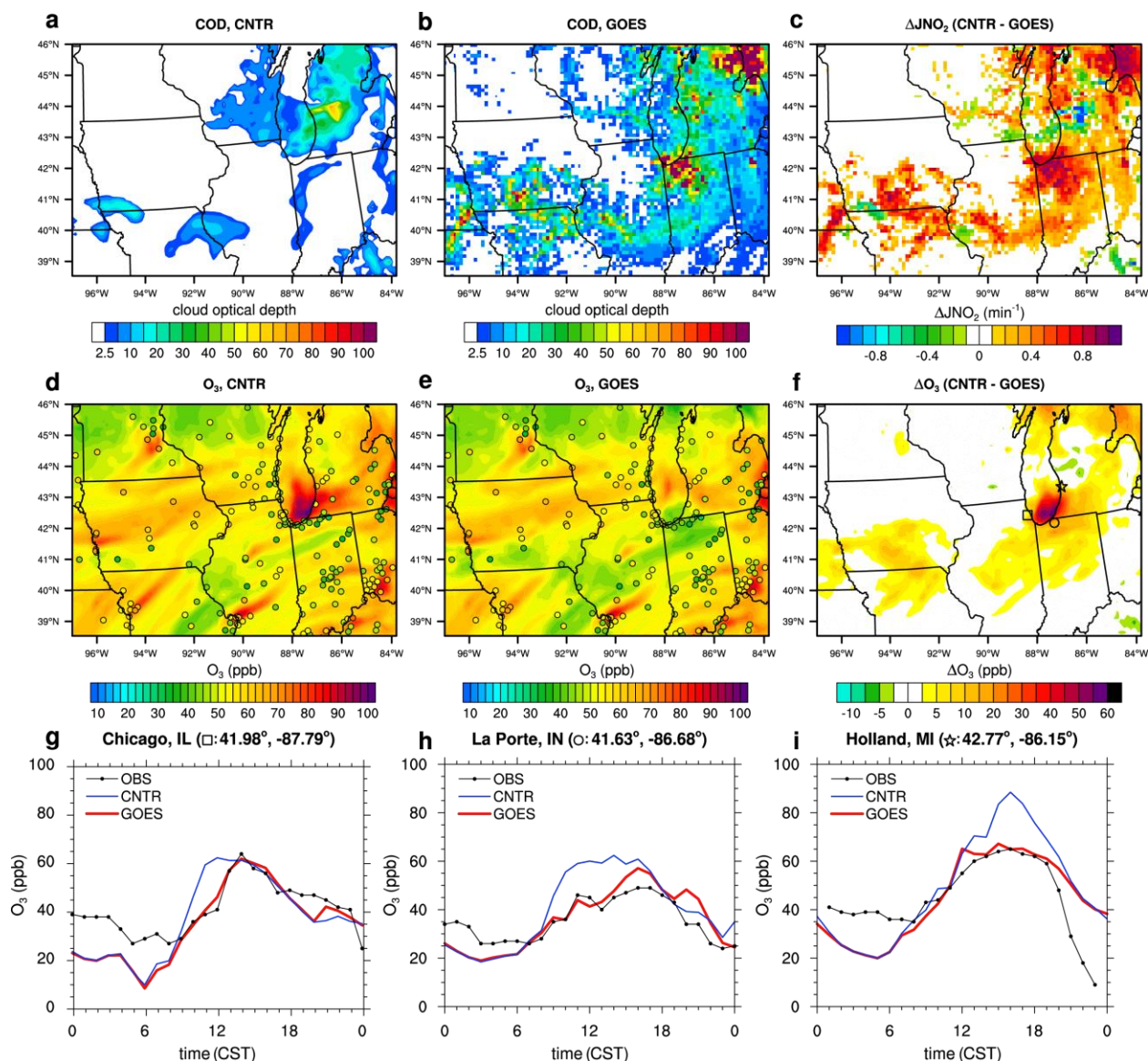
Fig. 4. Horizontal distributions of cloud optical depth at 13 CST (= 19 UTC) 8 July 2013 (a) in

the CNTR simulation and (b) in the GOES simulation. Horizontal distributions of O_3 at 13 CST

8 July 2013 at the lowest model level (shaded) (d) in the CNTR simulation and (e) in the GOES

simulation. The circles indicate EPA ozone measurements. (c and f) Difference in JNO_2 and O_3,

respectively, between the simulations (i.e., CNTR simulation minus GOES simulation). (g, h,

and i) Time series of O_3 at the square (Chicago, IL), circle (La Porte, IN), and star (Holland, MI)

that are marked in (f), respectively.

909
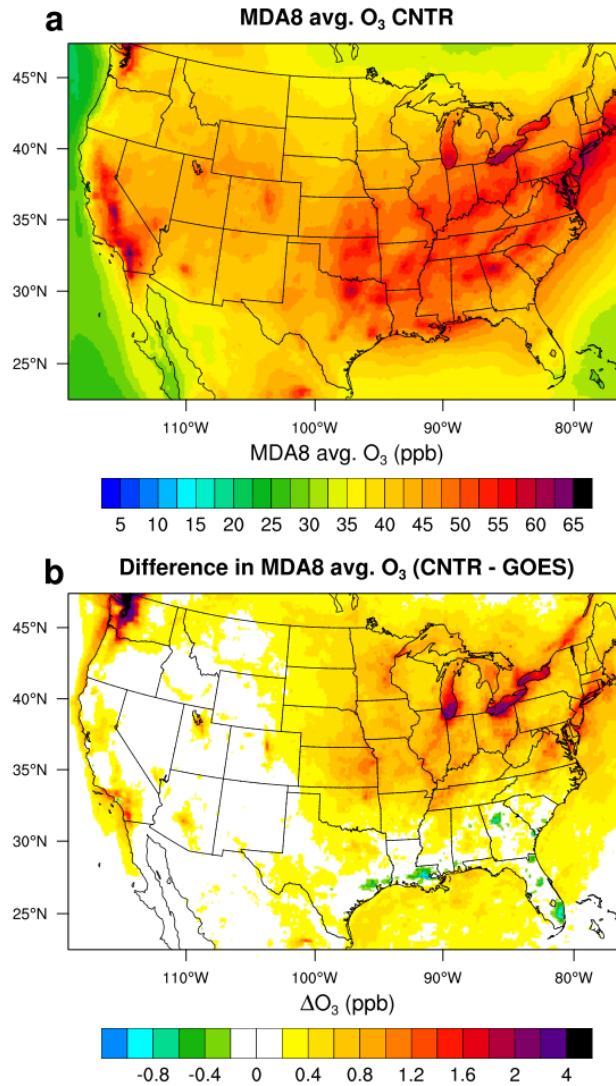
Fig. 5. (a) Spatial distribution of maximum daily 8-h average O_3 (MDA8 O_3) at the lowest model level averaged over the whole analysis period in the CNTR simulation. (b) Difference in MDA8 O_3 at the lowest model level between the control and GOES simulations (i.e., CNTR minus GOES).

910
911
912
913

914

915

916

917
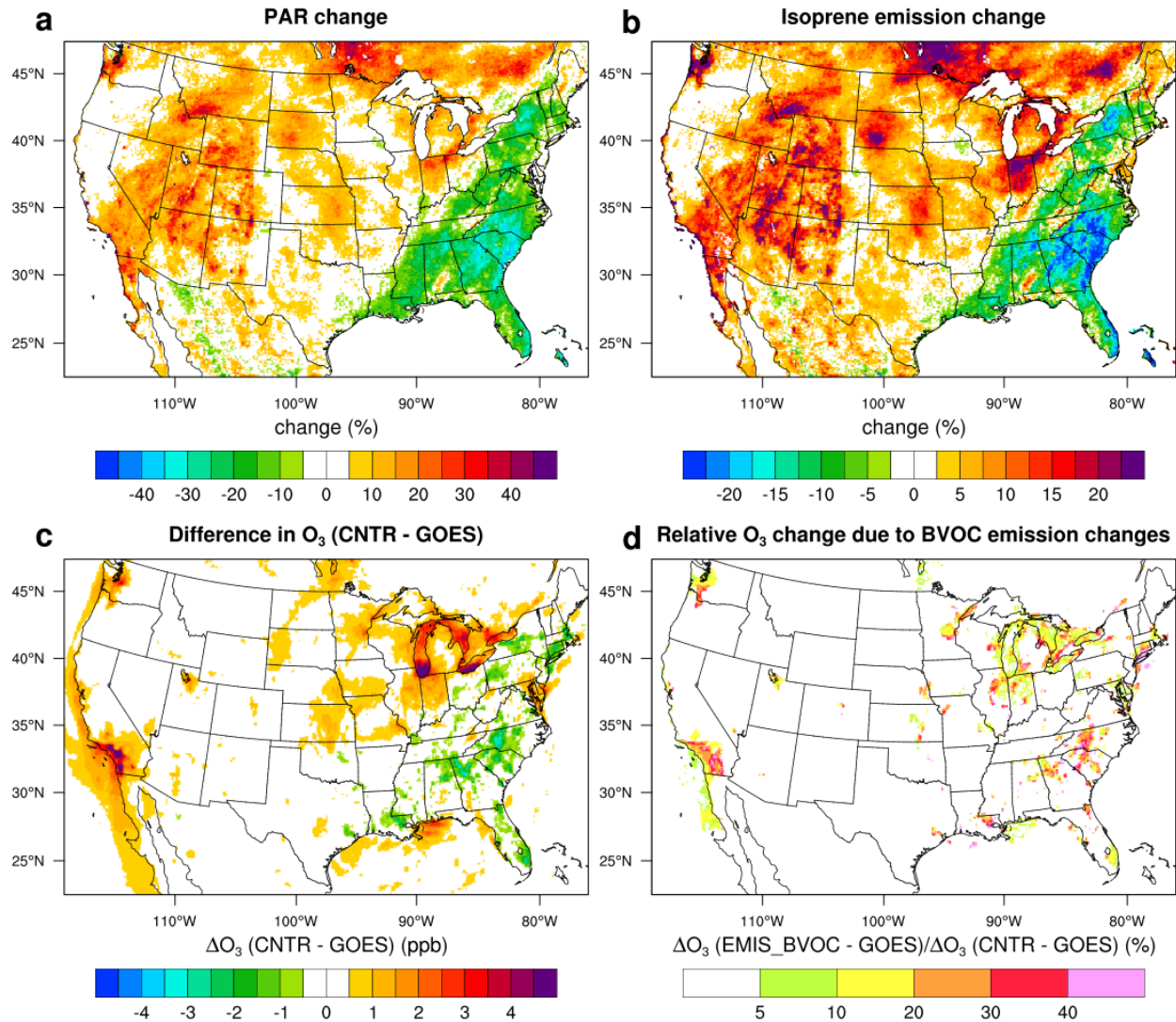
Fig. 6. Spatial distributions of (a) PAR change and (b) isoprene emission change from biogenic sources between EMIS_BVOC and GOES simulations, (EMIS_BVOC–GOES)/GOES, averaged over the period of 3–12 July 2013. (c) Difference in O_3 between the CNTR and GOES simulations. (d) Ratio of O_3 difference between EMIS_BVOC and GOES simulations to O_3 difference between CNTR and GOES simulations, i.e., ΔO_3(EMIS_BVOC–GOES)/ΔO_3 (CNTR–GOES). Note that the grids that have considerable O_3 difference between CNTR and GOES simulations (> 1 ppb) are depicted in (d).

925
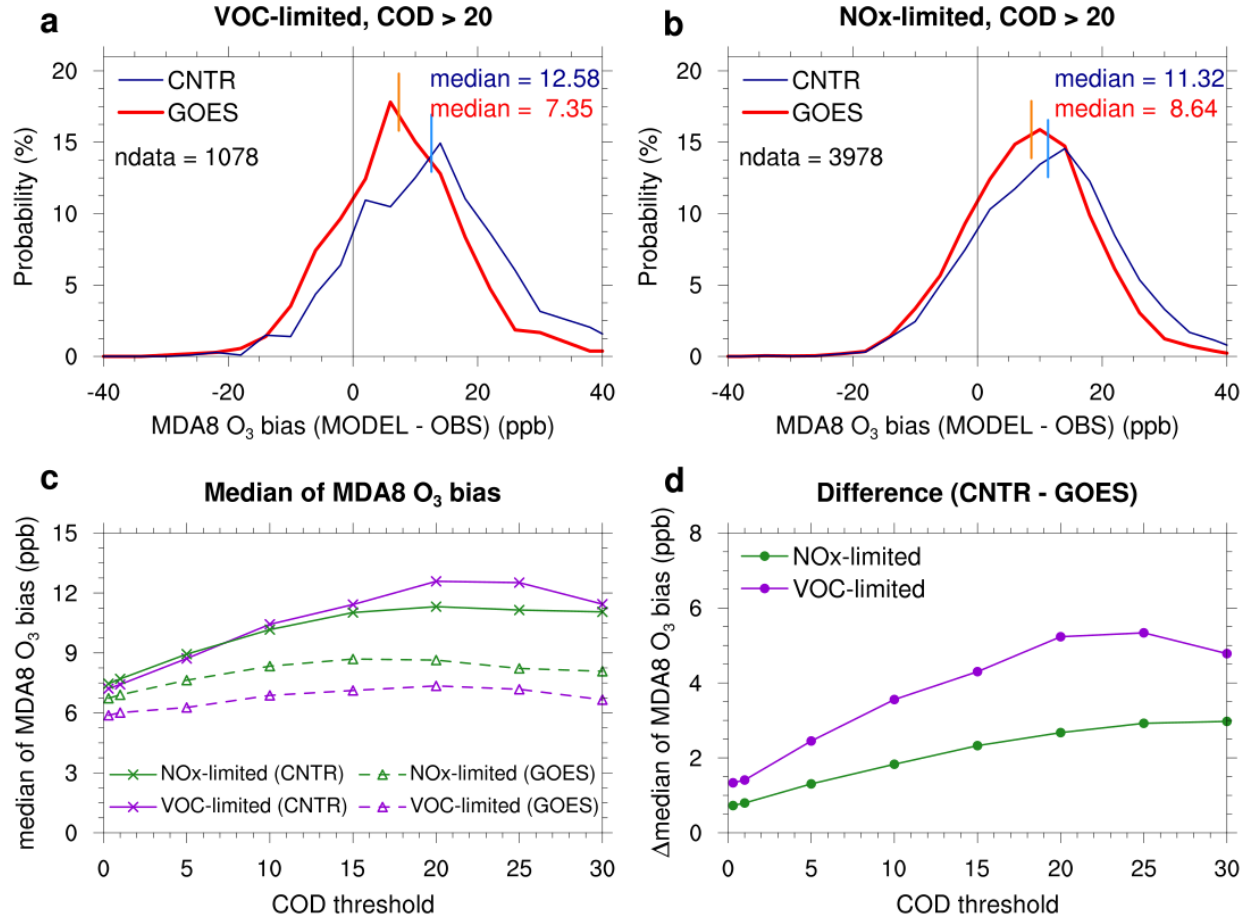
Fig. 7. (a) Probability density function of maximum daily 8-h average (MDA8) O_3 bias (model

value minus observation value) for VOC-limited regime under cloudy sky conditions defined

with COD threshold of 20. (b) Same as (a), but for NO_X-limited regime. (c) Median values of

MDA8 O_3 bias with respect to COD threshold in the CNTR simulation (solid lines with cross

marks) and in the GOES simulation (dashed line with triangles) for VOC-limited (purple color)

and NO_X-limited regimes (green color). (d) Difference in median values of MDA8 O_3 bias

between the two simulations with respect to COD threshold (i.e., CNTR minus GOES).

933

934

935
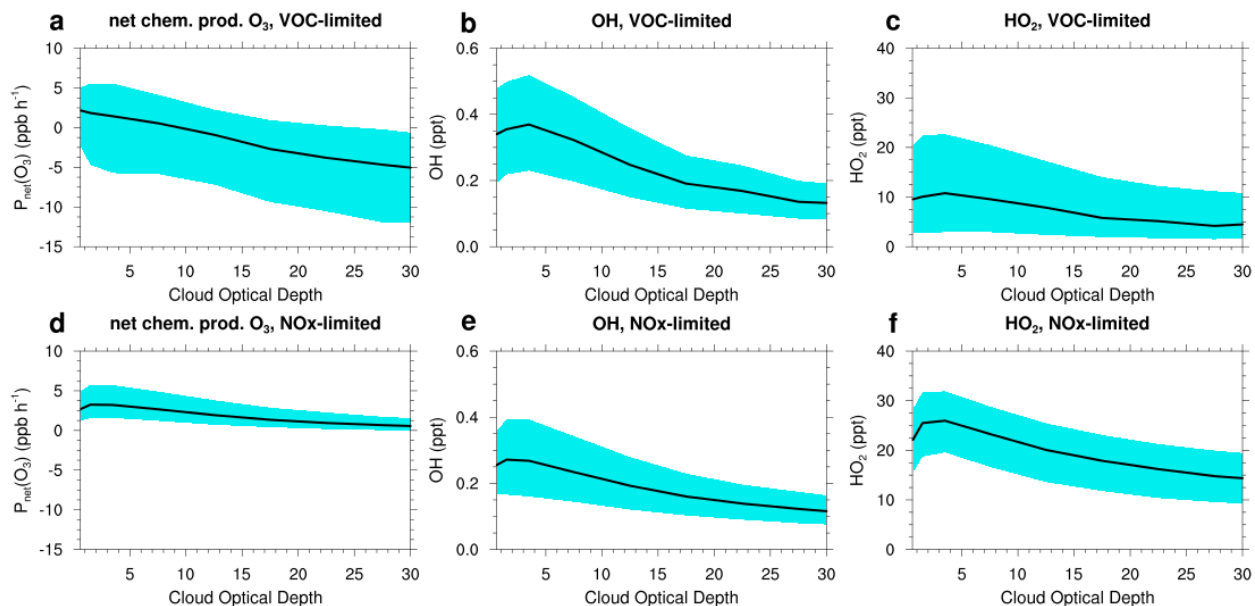
Fig. 8. (a) Net chemical production of O_3, (b) OH concentration, and (c) HO_2 concentration with variations of cloud optical depth for VOC-limited regime. The black line indicates the median and cyan shading indicates the 25 and 75 percentiles. Similar variables are shown for the NO_X-limited regimes (d, e, and f).

936

937

938

939

940

941

942

943

944

945
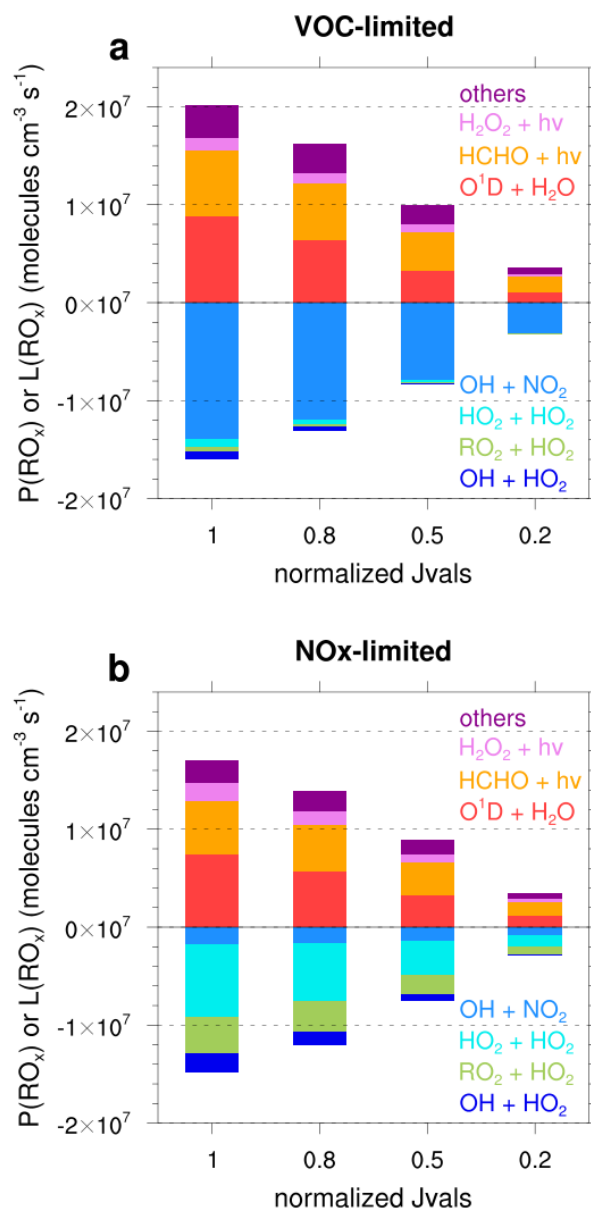
Fig. 9. Results of box modeling for production and loss rates of ROx (= OH + HO$_2$ + RO$_2$)

radicals. "Others" in the legend indicates the photolysis of VOCs and reactions between alkenes

and O$_3$. The value of 1 of normalized Jvals on *x*-axis indicates the photolysis rates for clear sky

conditions.

950